

Adjoint-Based Boundary Condition Sensitivity Analysis

Zhen Zhang,^{*} Yinbo Mao,[†] Xinrong Su,[‡] and Xin Yuan[§]
Tsinghua University, 100084 Beijing, People's Republic of China

<https://doi.org/10.2514/1.J061307>

Turbine performance in modern aeroengines is heavily affected by the nonuniform temperature distribution generated in the combustor. The conventional method to study the effect of nonuniform boundary conditions (BCs) is to compare flowfields and performance metrics with the nonuniformity at several typical positions. A much more efficient and intuitive method to analyze the BC sensitivity is proposed in this paper. An inlet guide vane is analyzed as a demonstration. The sensitivity analysis is achieved by pointwise derivatives of objectives with respect to inlet BCs, which are obtained by discrete adjoint method. Furthermore, to study the variation of gradients, a random sampling method that is based on the Gaussian process is proposed to explore the high-dimensional parameter space. When the gradient is invariant within the parameter space, the relationship between objectives and BCs is linear, and the effect of any perturbation of BCs can be directly predicted. In this case, the computational cost of the sensitivity analysis is drastically reduced to one computational fluid dynamics and one adjoint simulation. Interestingly, some gradients are nearly invariant across the parameter space. When the gradient varies, the active subspace method is introduced to reduce the number of dimensions. Then, several models, including the kriging, gradient-enhanced kriging (GEK), and Taylor expansions, are compared to predict objectives. The ordinary kriging model is recommended for its accuracy and stability. The GEK model can also predict the gradient and is a good choice for small BC variations. The method presented here offers a paradigm that extends the gradient-based sensitivity analysis to the global sense, which is suitable for high-dimensional problems such as BCs and spatially varying model parameters.

Nomenclature

A_i	=	grid element area
\mathbf{B}	=	boundary condition vector
m	=	mass flow rate, kg/s
P	=	pressure, Pa
T	=	temperature, K
U	=	velocity magnitude, m/s
γ	=	loss coefficient
ρ	=	density, kg/m ³

Subscripts

inlet	=	vane inlet
outlet	=	vane outlet
t	=	stagnation
vane	=	vane surface

I. Introduction

IN THE well-known problem of the interaction between the combustor and the inlet guide vane (IGV), researchers try to understand the influence of nonuniform inlet conditions and to find the optimal relative position between the combustor and the IGV [1]. The conventional method to study this problem is to experimentally or numerically compare IGV performances with different nonuniform inlet boundary conditions (BCs). Smith et al. [2] calculated a stage of a high-pressure turbine with a hot streak aligned or misaligned to the vane leading edge. They concluded that the aligned hot streak increased the vane thermal load while reduced the nonuniformity of the blade inlet. Flow angles and pressure loads were not affected by the hot streak. Gaetani and Persico [3] measured the velocity and temperature fields of a high-pressure turbine stage with an inlet hot

streak at four different circumferential positions. Results showed that different positions lead to different hot streak migration, temperature attenuation, and stator thermal stress. In Ref. [4], an unsteady numerical simulation was performed to study the co-effect of the turbulence intensity and the hot streak positions on a high-pressure turbine. Hot streak positions were shown to affect both the temperature and heat transfer coefficient at blade surfaces. These works directly compared different designs and offered insight into the flow mechanism behind hot streak migration and its influence. However, it is difficult for these comparison-based methods to determine the spatially distributed sensitivity and to predict the performance of arbitrary forms of the BC distribution. The optimal design may be missed in such surveys.

Thanks to the adjoint method, high-dimensional gradients can be obtained with the cost independent of the dimension. As far as the authors know, Su and Yuan [5] first used the adjoint method to study the sensitivity of the inlet BCs. They calculated the gradient of performance metrics, such as the mass flow rate, entropy rise, and loss coefficient, to inlet total temperature and total pressure. They drew sensitivity distributions at the inlet surface and quantitatively illustrated the effect of inlet BCs on the loss. They introduced the gradient-based strategy to analyze the BC sensitivity, which overcame the defect of the conventional comparison-based method. Based on gradients, the effect of any BC perturbations can be determined and the optimization direction is clearly indicated.

However, the major defect of the gradient-based sensitivity analysis is the local linear approximation. It brings large uncertainties when applied to large parameter space. To address this issue and to develop a gradient-based global sensitivity analysis, a random sampling method that is based on the Gaussian process is proposed to search the high-dimensional space with a limited number of samples. When the gradient is invariant within the space, the linear assumption is globally valid and the objectives can be directly calculated based on the gradient. This is the ideal situation, where the derivative distinctly reveals the flow mechanisms and optimal designs. When the gradient significantly varies within the space, the linear assumption is not valid and the relationship between BCs and performance metrics is highly nonlinear. In this case, the local gradient is of little value for prediction. To predict the objectives, the active subspace method (ASM) [6] is introduced to reduce the number of dimensions by constructing an active subspace where the objective varies the most. The ASM was proposed to reduce the dimension of a high-dimensional space by conducting singular value decomposition (SVD) to the gradient vectors. It has been applied to construct a surrogate model for shape optimization [7] and to build an engineering map

Received 23 September 2021; revision received 2 December 2021; accepted for publication 27 December 2021; published online 25 January 2022. Copyright © 2022 by the American Institute of Aeronautics and Astronautics, Inc. All rights reserved. All requests for copying and permission to reprint should be submitted to CCC at www.copyright.com; employ the eISSN 1533-385X to initiate your request. See also AIAA Rights and Permissions www.aiaa.org/randp.

*Doctoral Student.

[†]Postdoc Research Associate.

[‡]Assistant Professor; suxr@mail.tsinghua.edu.cn (Corresponding Author).

[§]Professor.

for the design of gas turbine fans [8]. After the dimension reduction, several models, including kriging, gradient-enhanced kriging (GEK), and Taylor expansions, are compared. The ordinary kriging model is recommended for its accuracy and stability. The GEK model can also predict the gradient and is a good choice for small BC variations. So far, the objectives can be fast predicted even with varying gradients. The gradient-based property and the efficient dimension reduction of the ASM make this method a bridge to link local gradients and the global search. In this way, a gradient-based global sensitivity analysis is established.

This paper is organized as follows. The second section illustrates methods and the validation. The third section discusses the global variation property of the gradient within the parameter space. In the fourth section, the ASM dimension reduction and the model comparison are illustrated. The conclusion is at last.

II. Method and Validation

The VKI inlet guide vane [9] is studied in this work as a demonstrative case. Two-dimensional compressible Reynolds-averaged Navier-Stokes (RANS) calculation is performed using the SU2 solver [10]. In the direct problem (i.e., solving the RANS equation), the Jameson-Schmidt-Turkel (JST) convective scheme [11] and the Spalart-Allmaras (SA) turbulence model [12] are adopted. In the adjoint problem, the discrete adjoint solver in SU2 [13] is used, which is based on the automatic differentiation package CoDiPack [14].

A. Gradient Calculation

In existing studies about the interaction between combustor and turbine blade, first a case with uniform inlet BC (denoted as \mathbf{B} hereafter) is computed. Then several cases with simulated nonuniform BCs $\mathbf{B} + \delta\mathbf{B}$ are computed, and the difference between the uniform inlet and nonuniform inlet is important to the design of a reliable turbine blade. Inspired by the adjoint method widely used in the design optimization [15,16], it is realized that this problem can also be solved with the adjoint sensitivity. Different from the adjoint optimization for which the design variable is the geometrical parameters, in this work the BCs are treated as the design variables for which the adjoint sensitivities are computed.

Basic ideas of the discrete adjoint solver are listed here for completeness. Readers are referred to reference [13] for details. With inlet BCs (\mathbf{B}) being the design variables, the gradient of any performance metric J with respect to design variables is given by the Lagrangian method. The flow constrain in form of fixed-point is

$$\mathbf{U}(\mathbf{B}) = \mathbf{G}(\mathbf{U}(\mathbf{B}), \mathbf{B}) \quad (1)$$

where \mathbf{U} is the vector of flow state variables. The Lagrangian is

$$L = J + \lambda^T(\mathbf{G} - \mathbf{U}) \quad (2)$$

where λ is the Lagrange multiplier vector. Therefore, the gradient is given by

$$\frac{dJ}{d\mathbf{B}} = \frac{dL}{d\mathbf{B}} = \frac{\partial L}{\partial \mathbf{B}} + \frac{\partial L}{\partial \mathbf{U}} \frac{d\mathbf{U}}{d\mathbf{B}} \quad (3)$$

Choosing λ such that $\partial L / \partial \mathbf{U} = \mathbf{0}$ yields the adjoint equation

$$\lambda^T = \frac{\partial J}{\partial \mathbf{U}} + \lambda^T \frac{\partial \mathbf{G}}{\partial \mathbf{U}} \quad (4)$$

With the solved λ , the gradient can be determined as

$$\frac{dJ}{d\mathbf{B}} = \frac{\partial L}{\partial \mathbf{B}} = \frac{\partial J}{\partial \mathbf{B}} + \lambda^T \frac{\partial \mathbf{G}}{\partial \mathbf{B}} \quad (5)$$

Based on the automatic differentiation technique, Eqs. (4) and (5) can be solved, and the gradient of any performance metric to the design variables can be obtained conveniently.

B. Grid Dependence Check

The grid dependence check of the direct problem is performed. The inlet total temperature of the VKI vane is 280 K, the inlet total pressure is 1.4 bar, and the outlet pressure is 0.92755 bar. Three sets of meshes are used, which contain 8000, 32,000, and 128,000 elements, respectively. The coarse mesh is shown in Fig. 1.

Figure 2 shows the comparison of the isentropic Mach number distributions among three sets of meshes with the experiment in [9]. Numerical results coincide with the experiment, and they differ mainly at the Mach peak on the suction side. All of these meshes are believed sufficient for the direct calculation.

As for the discrete adjoint calculation, each adjoint solution is based on the corresponding converged direct (RANS) solution. Three objectives are studied in this work, which are the area-averaged temperature at the vane surface $T_{\text{mean,vane}}$, the outlet total pressure loss coefficient $\gamma_{\text{Pt,outlet}}$ as defined in Eq. (6), and the passage mass flow rate m_{outlet} .

$$\gamma_{\text{Pt,outlet}} = \frac{P_{t,\text{inlet}} - P_{t,\text{outlet}}}{\frac{1}{2}\rho U_{\text{outlet}}^2} \quad (6)$$

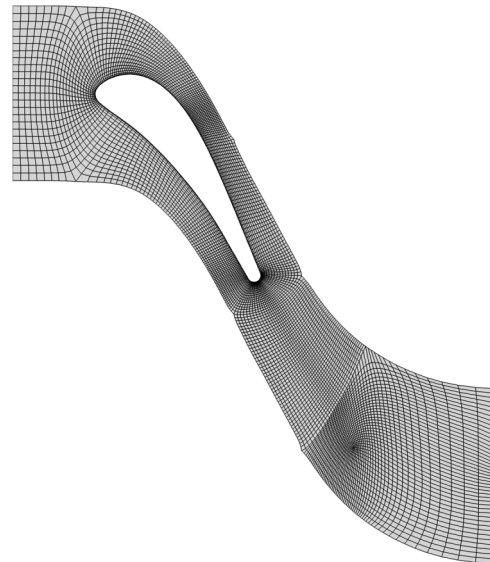


Fig. 1 Coarse mesh used for mesh convergence check.

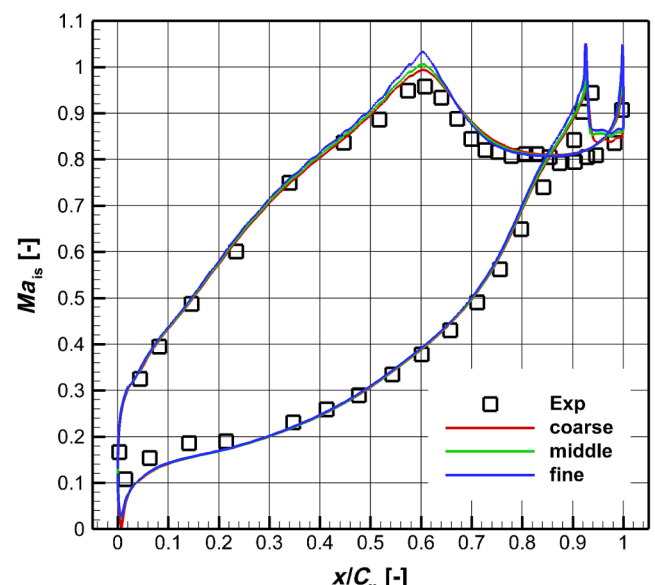


Fig. 2 Isentropic Mach number distribution, compared with the experiment in [9].

Note that all terms in Eq. (6) are involved in the derivation process. In the discrete adjoint solver, the inlet total temperature and inlet total pressure at all inlet boundary points are used as the independent variables, and the derivative of the objective to these independent variables can be obtained. Although both total temperature and total pressure are registered as design variables during the calculation, they will be studied separately. Besides, three objectives will also be studied separately. So the derivatives in the following content can be regarded as a vector, whose dimension equals the number of mesh points at the inlet boundary. Figure 3 shows the sensitivities of the three objectives to the inlet total temperature on different meshes. The vertical axis represents the nondimensional pitchwise position of the inlet surface (see Fig. 1), and the horizontal axis represents the sensitivity per unit area, as shown in Eq. (7).

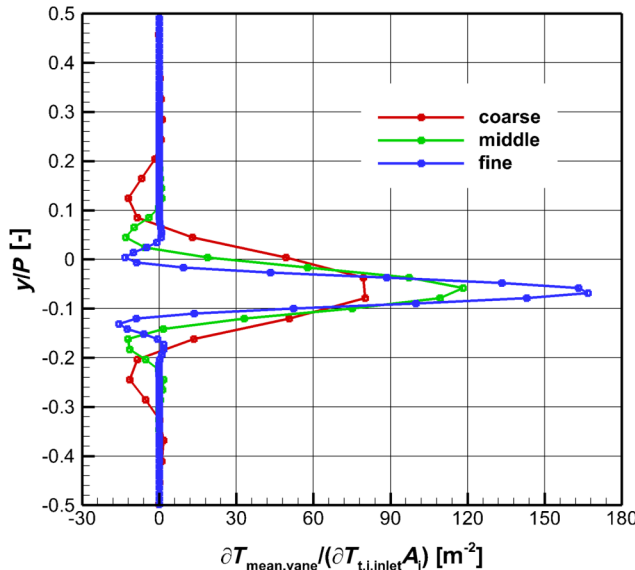
$$\frac{\partial T_{\text{mean,vane}}}{\partial T_{t,i,\text{inlet}} A_i} = \frac{1}{A_i} \frac{\partial T_{\text{mean,vane}}}{\partial T_{t,i,\text{inlet}}} \quad (7)$$

where $T_{t,i,\text{inlet}}$ is the total temperature at the mesh grid of the inlet surface, and A_i is the area of the corresponding mesh element. Because the mesh resolutions are different in three sets of meshes,

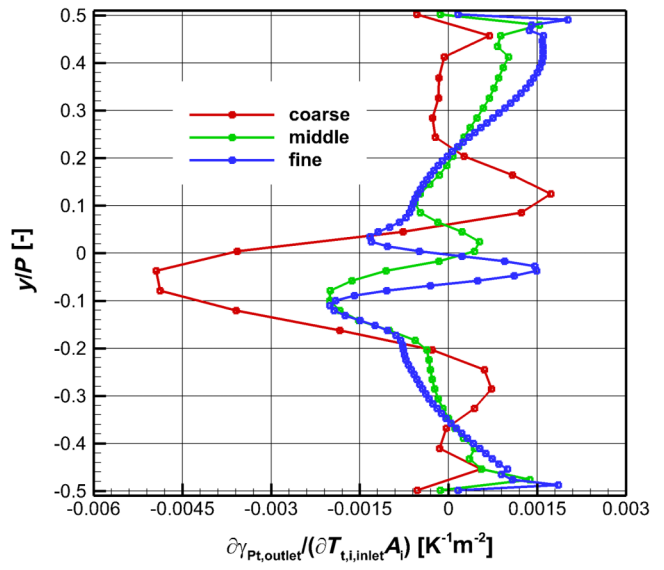
the derivatives are normalized by the element area. When the differential of both inlet total temperature and total pressure are considered, the total differential of the objective is

$$dT_{\text{mean,vane}} = \sum_i \frac{\partial T_{\text{mean,vane}}}{\partial T_{t,i,\text{inlet}}} dT_{t,i,\text{inlet}} + \sum_j \frac{\partial T_{\text{mean,vane}}}{\partial P_{t,j,\text{inlet}}} dP_{t,j,\text{inlet}} \quad (8)$$

Besides, due to the existence of the periodic BC, the two points at the periodic boundaries contribute together to the sensitivity, and the derivative values are about half of the neighboring points. From Fig. 3, the mesh resolution distinctly affects derivative distributions. For regular distributions such as the derivative of the vane temperature and the mass flow rate, the coarse mesh predicts the correct trend. However, for those irregular distributions such as the derivative of the loss coefficient, the coarse mesh predicts a very different derivative distribution from finer meshes. The derivative distributions seem to be more sensitive to the mesh resolution than overall performance metrics. However, gradients obtained from each mesh are validated against finite-difference results (shown in Sec. II.D), which means that if the objective is properly predicted in the direct calculation, the objective difference can be also predicted by the gradient,



a) Sensitivity of vane temperature



b) Sensitivity of loss coefficient

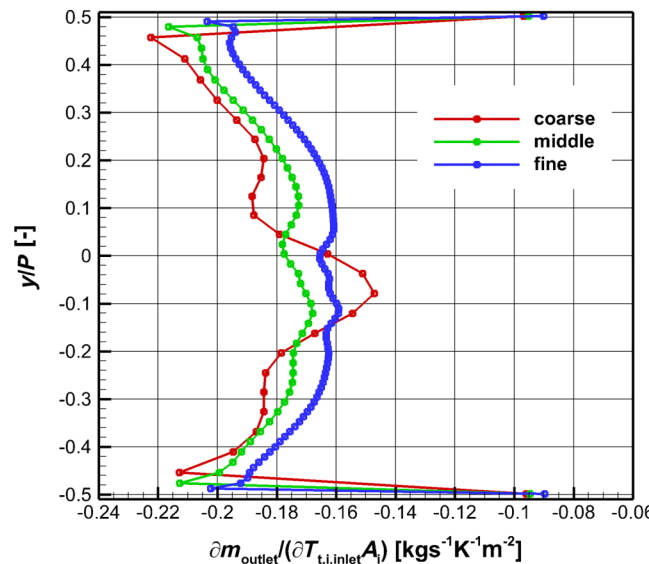


Fig. 3 Sensitivity of objective to inlet total temperature on different meshes.

despite slight dependency on the mesh resolution. Therefore, the middle mesh with 32,000 elements is chosen, because it can predict the right trend.

C. Sampling Method

The random sampling within the high-dimensional parameter space is introduced here. There are 49 grid points at the inlet boundary surface of the middle mesh. The inlet total temperature (or total pressure) can be regarded as a vector in a 49-dimensional space. Each dimension corresponds to the total temperature at one grid point. When the dimension increases, much more samples are required. Therefore, it is important to reduce the dimension. Note that the inlet BC is smooth and periodic. The smoothness means that there is a distinct correlation among neighboring dimensions, which decays with the distance. The periodic property means that there is also a strong correlation between points a period apart. These correlations among dimensions reduce the freedom degree in the parameter space, so it is possible to use a moderate number of samples to fill the space. Therefore, the Gaussian process with a constant mean and a periodic kernel function [shown in Eq. (9)] is used to represent the inlet BC. It satisfies both the smooth and the periodic properties.

$$\text{Cov}(x_1, x_2) = \exp\left(-\frac{2}{l^2} \sin(|x_1 - x_2|\pi)\right) \quad (9)$$

The parameter l is chosen to control the flatness of samples. Small l reduces the correlation among different dimensions while large l leads to flat distributions; l also affects the representation ability of the samples. Smaller l leads to samples with stronger variations. These samples can represent BCs with more rapid variation than those flat samples from larger l . The value of l should be around one, and $l = 1.0$ is chosen here. Besides, in order to fill the parameter space, a rejection method is adopted to guarantee that the Euclidean distance between arbitrary two samples is larger than a predefined threshold:

$$\|\mathbf{B}_1 - \mathbf{B}_2\|_2 > \text{threshold} \quad (10)$$

where \mathbf{B} is the sample vector that represents the inlet BCs. Given the dimension, different sample distances lead to different numbers of samples. Figure 4 shows a sampling result. In the sampling process, two uniform boundaries of the parameter space are sampled first, which are named case 0 and case 1. They are also the upper and lower

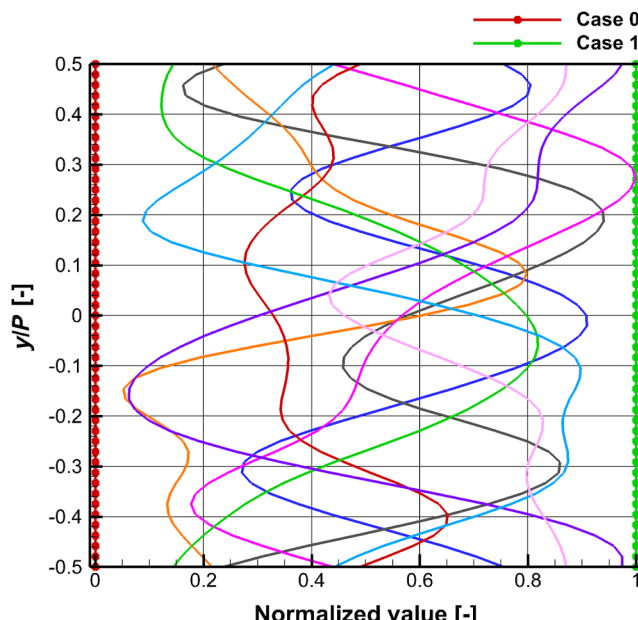


Fig. 4 Sampling results of the Gaussian process and the rejection method.

bounds of the sampling process. Then the random sampling starts. If the new sample does not exceed two boundaries and satisfies the distance criterion, it will be accepted and otherwise rejected. After 30,000 steps, there is nearly no new sample added and the random sampling stops. These nondimensional samples are then used to generate the inlet BCs. This sampling method uses the sample's spatial property where there are distinct correlations among different dimensions and introduces the Gaussian process to conveniently construct samples. By doing so, the number of samples is drastically reduced compared with conventional sampling strategies such as Latin hypercube sampling.

D. Gradient Validation

The gradient is compared with the finite difference to validate its accuracy. The gradient is of high dimension, so it is difficult to validate it in each dimension. Therefore, the objective differences calculated by the gradient and by the finite difference are compared to validate the gradient. The gradient of the averaged vane temperature to the inlet total temperature is shown here. Using the above sampling method, five samples with $\Delta T_t = 1 \times 10^{-4}$ K are used for the test. Between arbitrary two cases, the finite difference of the objective is calculated and compared with $\sum_i \Delta T_{t,i,\text{inlet}} \partial T_{\text{mean,vane}} / \partial T_{t,i,\text{inlet}}$. The relative error of the objective difference is shown in Table 1. The maximum relative error is 7.61×10^{-7} , showing satisfactory accuracy of the gradient.

III. Global Variation of Sensitivity

In this work, it is aimed to reveal flow mechanisms within the large parameter space. However, the gradient is inherently a local value and may vary in the parameter space. In this section, the variation property of the gradient is studied, and its invariance is regarded as a precondition to directly use the gradient for prediction.

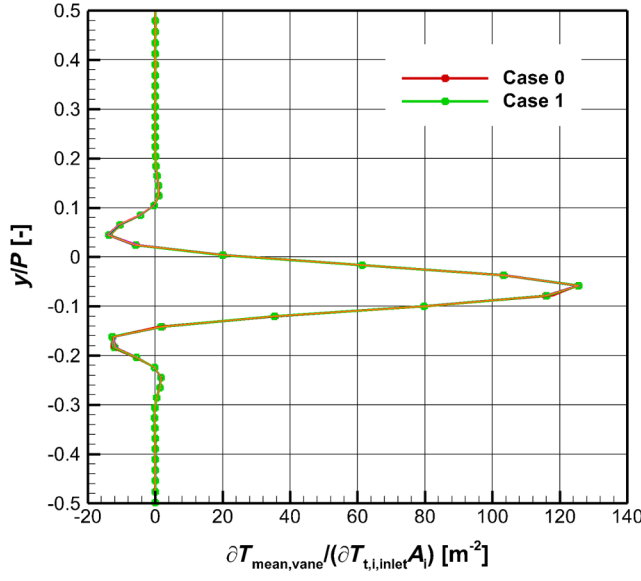
A. Sensitivity to Inlet Total Temperature

According to the sampling method, 17 samples are used to study the variation property of the sensitivity of the averaged vane temperature and the mass flow rate to the inlet total temperature. The deviation range of the independent variable is $\Delta T = 20$ K. Figure 5 shows the resultant sensitivities of the 17 cases. Surprisingly the sensitivity of the vane temperature almost keeps the same with the variation of independent variables. The sensitivity of the mass flow rate varies slightly and mainly within the range enclosed by the two uniform boundaries.

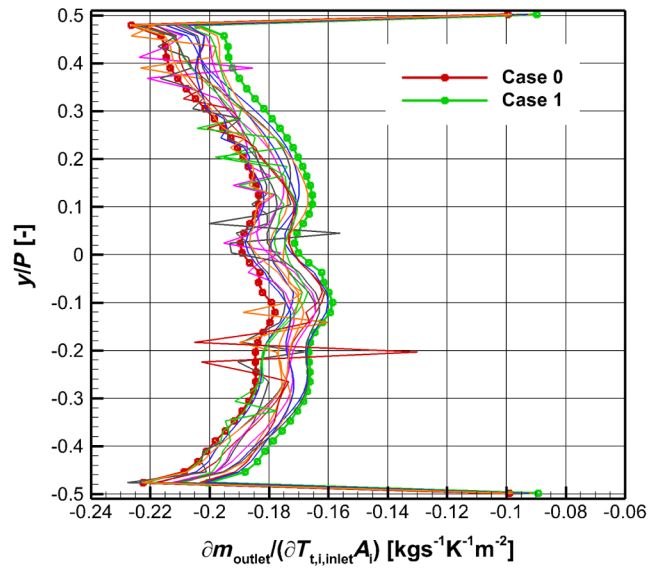
Following the strategy of the gradient validation, the objective differences calculated by the finite difference between every two samples and by the corresponding gradients are compared, and the relative errors (absolute values) are shown in Fig. 6. The horizontal axis "index" refers to the index of these comparisons between every two random samples. The gradient of the averaged vane temperature is almost invariant within the range, so errors are quite low, most of which are below 1%. The gradient of the mass flow rate varies slightly within the range, so most of the relative errors are less than 10%. Note that it is the error of the objective difference. Given a baseline and the corresponding gradient, if the gradient is almost invariant, we can predict the objective of arbitrary inlet distributions by adding the predicted difference to the baseline value with a quite satisfactory accuracy. And in this case the computational cost of the sensitivity analysis is drastically reduced to only one computational fluid dynamics and one adjoint simulation, showing the strength of this gradient-based method. The sensitivity of the vane temperature is positive at the middle, where the fluid flows and impinges at the vane leading edge. The relative position between the inlet boundary and the IGV is shown in Fig. 1. The positive value here is very natural, showing that a hot streak located here will increase the vane temperature, just as found in reference [2]. The zero value facing the vane passage shows that hot streaks located there will not diffuse to influence the vane temperature. It is quite counterintuitive that there are two regions where the sensitivity is negative, meaning that a hot streak located there will reduce the vane temperature. This

Table 1 Relative error of $\Delta T_{\text{mean,vane}}$

	Case 0	Case 1	Case 2	Case 3	Case 4
Case 0	— —	-3.81×10^{-9}	-3.56×10^{-9}	-7.90×10^{-7}	-7.83×10^{-9}
Case 1	-2.36×10^{-9}	— —	-2.48×10^{-9}	4.93×10^{-8}	4.15×10^{-9}
Case 2	-2.97×10^{-9}	-2.50×10^{-9}	— —	7.05×10^{-8}	1.36×10^{-8}
Case 3	7.61×10^{-7}	-5.39×10^{-8}	-7.56×10^{-8}	— —	-1.06×10^{-7}
Case 4	-2.33×10^{-9}	-4.05×10^{-9}	-6.15×10^{-9}	9.87×10^{-8}	— —

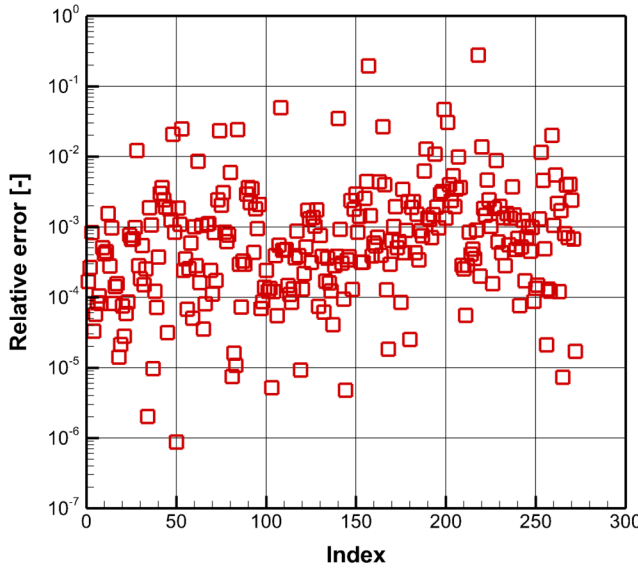


a) Sensitivity of vane temperature

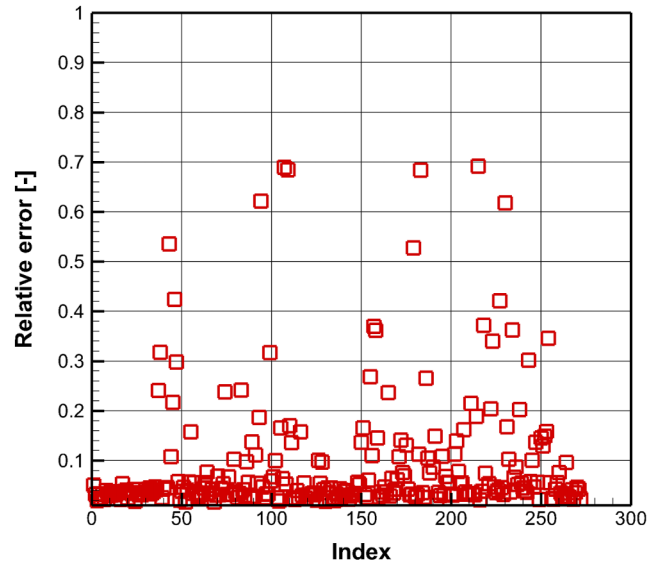


b) Sensitivity of mass flow

Fig. 5 Sensitivity of objectives to inlet total temperature from random sampling.



a) Averaged vane temperature



b) Mass flow rate

Fig. 6 Relative error of the difference of objectives.

phenomenon is hardly found without a gradient-based sensitivity analysis. As for the sensitivity of the mass flow rate, the negative value means that higher inlet total temperature leads to a lower mass flow rate, which is due to the reduced density. The reduction effect is more significant when the hot streak is facing the vane passage.

Here is an example to show the strength of this adjoint-based BC sensitivity analysis. The interface of the combustor and the IGV is characterized by a hot streak, which is due to the nonuniform combustion. The relative position of the hot streak and the vane is an important design problem. From Fig. 5a it can be found that there are

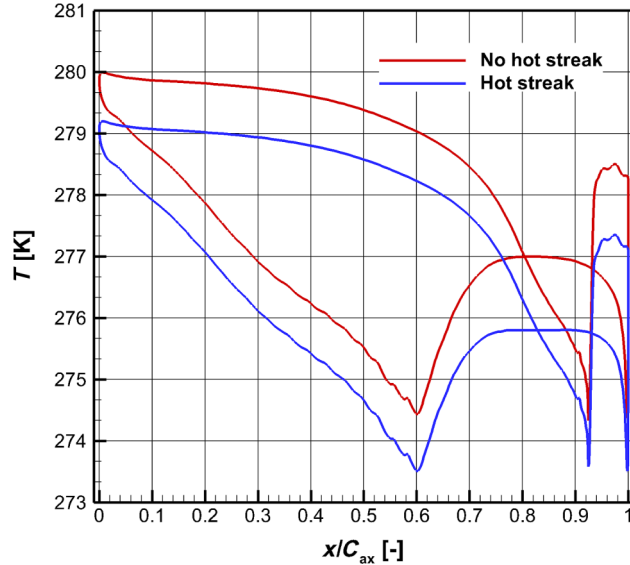


Fig. 7 Vane temperature with and without an inlet hot streak.

two regions where the sensitivity is negative, meaning that a hot streak located there will reduce the vane temperature. Therefore, a hot streak is added, which covers $-0.05 < y/P < 0.15$ with a sine shape and the intensity of 20 K.

Figure 7 shows the comparison of the vane temperature distribution with and without the hot streak. As predicted by the sensitivity analysis, the vane temperature is reduced by about 1 K. This case is two-dimensional and without intense turbulence, so this particular phenomenon cannot directly guide the real engineering design. However, the high-dimensional flow mechanism is very valuable and can bring subtle designs.

B. Sensitivity to Inlet Total Pressure

Fourteen samples are used to study the sensitivity of the total pressure loss coefficient and the mass flow rate to the inlet total pressure. Two ranges of the independent variable are tested, which are $\Delta P_t = 1\% P_{t0}$ and $\Delta P_t = 10\% P_{t0}$, where P_{t0} is the baseline inlet total pressure. The variation is negative to simulate the effect of swirls where the total pressure is lower.

Figure 8 shows sensitivities of the loss coefficient and the mass flow rate to the inlet total pressure with two ranges. Different ranges lead to different variation properties of the gradient. Gradients of both the loss coefficient and the mass flow rate vary slightly with the range of 1% and can be directly used for prediction. The gradient of the loss coefficient is positive facing the vane and negative facing the passage. The positive value means that higher total pressure here will increase the loss, which may be due to the intenser dissipation in the boundary layer. The negative value facing the vane passage means that higher total pressure here will reduce the loss. The gradient of the mass flow rate is always positive at the inlet surface because higher total pressure leads to higher velocity and thus a higher mass flow rate. This enhancement is more distinct at the location facing the vane passage. Related flow mechanisms can be further studied by analyzing the flowfield. On the contrary, gradients vary drastically and are not bounded by the two uniform boundaries (case 0 and case 1) with the range of 10%. It means that using the gradient of the baseline case for prediction will introduce huge errors and checking only the two uniform boundaries of the independent variable distributions cannot determine whether the gradient is invariant or not.

IV. ASM and Global Prediction

The variation of gradient in the parameter space is addressed in this section. The ASM method is introduced to reduce the dimension, and

then several methods, including the kriging model and the first-/second-order Taylor expansions, are tested to predict the objectives. A comprehensive test is conducted, where five positions are chosen to add total pressure valleys as shown in Fig. 9. They are in the sine form and cover the whole pitch. The variations are 1, 5, 10, and 20% of the baseline total pressure P_{t0} . The effects of valley position and intensity are both tested.

The basic idea of the ASM is to find a subspace in a high-dimensional space where the objectives vary the most. Gradients of the random samples are used to find such a subspace by SVD.

$$G = [g_1, \dots, g_n] = U\Sigma V^T \quad (11)$$

where G is the gradient matrix, g_i is the gradient vector, and n is the number of samples. Because of the descending order of the singular values, the first k left singular vectors of U can span a subspace where most variation happens.

$$U_k = \text{span}\{\mathbf{u}_1, \dots, \mathbf{u}_k\} \quad (12)$$

Different k leads to different accumulated singular values, and it controls the representing capacity of the subspace. In this work the first k singular values should account for at least 80% of the total singular value accumulation, and k is determined accordingly.

Figure 10 shows the singular value accumulations of the loss coefficient and the mass flow rate bases. They are calculated from 100 samples. It shows that singular values converge faster for the mass flow rate than for the loss coefficient. The first 9 bases for mass flow rate and the first 16 bases for loss coefficient are chosen to construct the active subspace.

Figure 11 shows the bases for the loss coefficient and the mass flow rate. For clarity, only the first five bases are shown. They are unit vectors and orthogonal to each other. They are sorted by singular values in descending order and are the most important directions in which the objective varies. The property of the objective determines the distribution of the singular values. Sometimes there are several dominant bases and the dimension reduction is natural, but sometimes many singular values are in the same order, leading to indistinct bases. Figures 11a and 11b are, to some extent, examples of these two situations. They are corresponding to Figs. 8b and 8d, respectively.

After determining such a subspace, any distribution of inlet BCs $\mathbf{B} \in \mathbb{R}^d$ can be projected to these bases to get a reduced-order representation $\mathbf{Y} \in \mathbb{R}^k$, where d is the inlet BC dimension, i.e., the number of inlet grid points, and k is much less than d .

$$\mathbf{Y} = U_k^T \cdot \mathbf{B} \quad (13)$$

The gradients $df/d\mathbf{B}$ can also be projected to these bases to get the dimension reduced.

$$df/d\mathbf{Y} = U_k^T \cdot df/d\mathbf{B} \quad (14)$$

Besides, the low-dimensional gradient vectors $df/d\mathbf{Y}$ can revert to the initial state conveniently.

$$df/d\mathbf{B} = U_k \cdot df/d\mathbf{Y} \quad (15)$$

These low-dimensional vectors \mathbf{Y} and $df/d\mathbf{Y}$ are then used to predict the corresponding objectives. To make full use of the information, several models are compared here. The first model is an in-house GEK model, which is based on the direct gradient enhancement strategy [17,18]. Unlike in [17], the GEK model here is dense and thus requires gradients at all sampling points and in all dimensions. \mathbf{Y} and $df/d\mathbf{Y}$ are used as input. Both the objective and its gradient at the test point can be predicted. The second model is an ordinary kriging model using the python pyKriging module [19]. The kriging model uses \mathbf{Y} as input and predicts objectives based on an interpolation strategy. The rest methods are all based on the

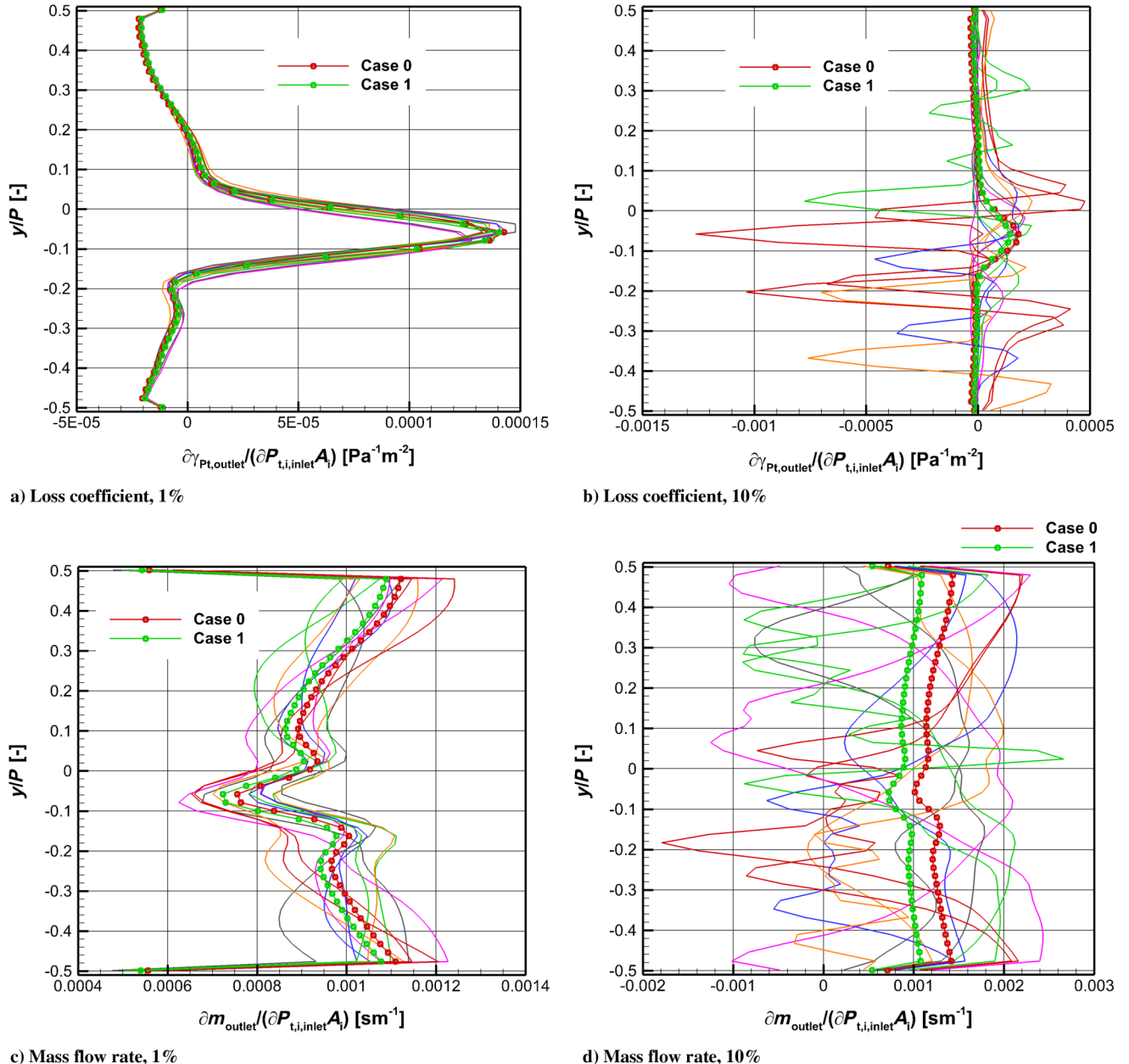


Fig. 8 Sensitivity of objectives to inlet total pressure from random sampling.

first/second order of Taylor expansions. Note that these expansion-based methods use \mathbf{B} and $df/d\mathbf{B}$ instead of \mathbf{Y} and $df/d\mathbf{Y}$ as input to avoid the truncation error introduced in the dimension reduction. The third model is the first-order expansion at the initial point, i.e., the baseline uniform sample case 1. This model directly uses the objective and the gradient at the uniform \mathbf{B}_0 to predict objectives

$$f = f|_{\mathbf{B}_0} + \Delta \mathbf{B}^T \cdot df/d\mathbf{B}|_{\mathbf{B}_0} \quad (16)$$

The fourth model is the first-order expansion at the nearest sampling point. This model first searches for the sampling point closest to the test point and then conducts the expansion there. The fifth model is the second-order expansion at the nearest sampling point \mathbf{B}_{near} . The well-known BFGS algorithm is used to approximate the Hessian matrix \mathbf{H} using 20 samples near the expansion point. The number of samples used in BFGS is determined by a parameter search. The objective is then calculated by

$$f = f|_{\mathbf{B}_{near}} + \Delta \mathbf{B}^T \cdot df/d\mathbf{B}|_{\mathbf{B}_{near}} + \frac{1}{2} \Delta \mathbf{B}^T \cdot \mathbf{H}|_{\mathbf{B}_{near}} \cdot \Delta \mathbf{B} \quad (17)$$

To build these models, 100 points are sampled using the Gaussian process sampling method, and the maximum deviation is $\Delta P_t = 10\% P_{t0}$. For the loss coefficient prediction, 16 bases are used to represent the parameter space. For the mass flow rate, nine bases are used.

Figures 12 and 13 compare the model prediction for loss coefficient and mass flow rate. The horizontal axis represents the five positions shown in Fig. 9. The real values at various ΔP_t and various positions are compared with model outputs. The “Grad init” is for the first-order expansion at the initial sampling point, “Grad near” is for the first-order expansion at the nearest sampling point, and “BFGS near” is for the second-order expansion at the nearest sampling point. Note that scales of the vertical axis are different. When the ΔP_t is small, the objective variation among different positions is also small and the axis is scaled up. In real engines the uniformity of inlet BCs is unfavorable and thus normally does not exceed 10%. The maximum

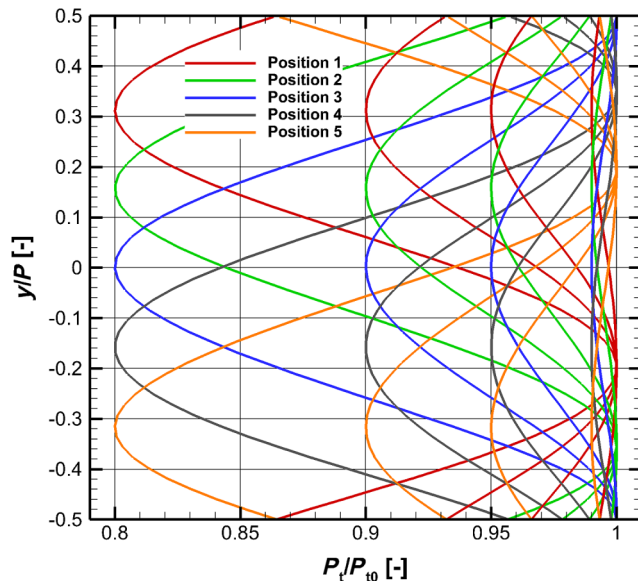


Fig. 9 Typical nonuniform total pressure distributions used for testing.

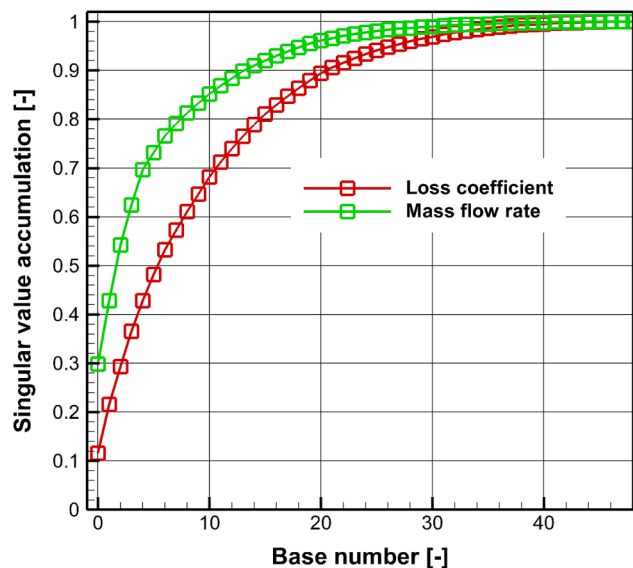
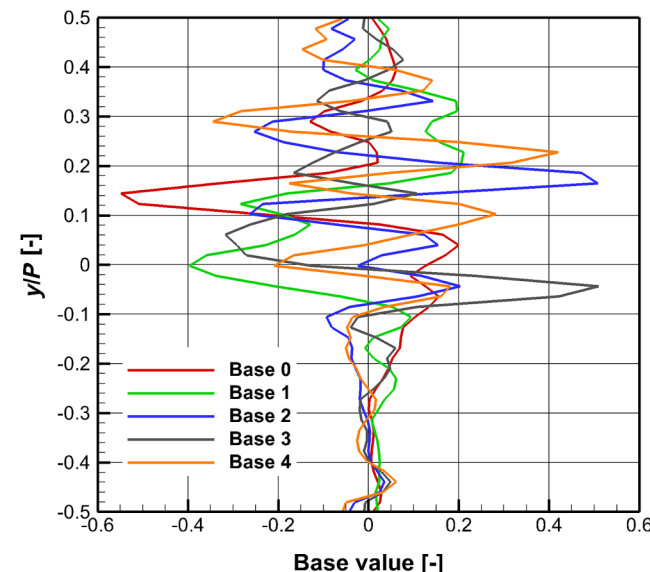


Fig. 10 Singular value accumulation of the ASM predictor.

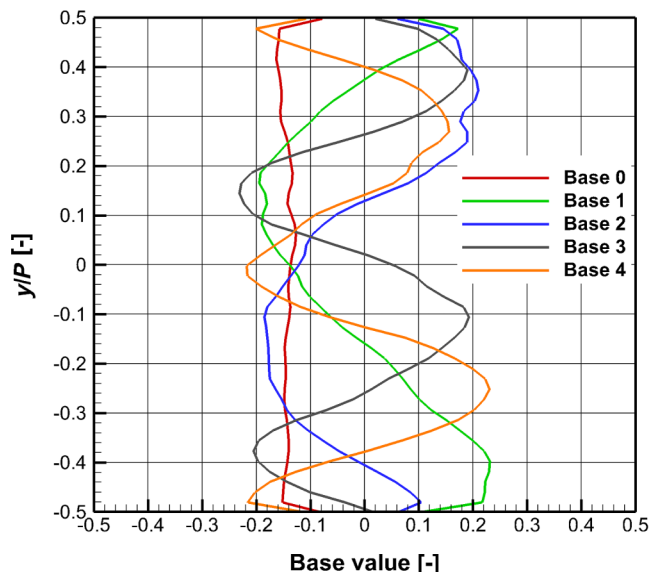


a) Bases for the loss coefficient

tested BC deviation is 20% and exceeds the sampling range (10%). The real values show that when total pressure valleys face the vane, i.e., positions 2–4, the loss is lower and the mass flow rate is higher, which agrees with the trend in Figs. 8a and 8c.

Figure 14 summarizes the relative errors of these models. Note that the vertical axis uses a logarithmic scale. For each ΔP_t , relative errors of each model at five positions are averaged. The “Real std” means the standard deviation of the real values at all 20 test cases divided by the mean value. This value represents the variation of objectives. Models are supposed to have errors much smaller than it, e.g., by one order of magnitude. In this case, the model is regarded as effective. Otherwise, the model error is too large and the prediction is meaningless. When the BC deviation is 1%, all of these models are effective. The GEK for mass flow rate shows the best accuracy. The initial first-order expansion is also accurate, showing that the linear assumption is valid in that range. When the BC deviation is 5%, two kriging models perform well. The initial first-order expansion is ineffective, showing that the linear assumption does not hold anymore. With the increase of the distance between the test point and the nearest sampling point, the two nearest expansions become less accurate. They are sensitive to this distance and thus are not stable for global prediction. When the BC deviation is 10%, which is also the limit of the training samples, the ordinary kriging model is effective. The nearest first-order expansion is also effective for mass flow rate. When the BC deviation is 20% and exceeds the sampling limit, no model is effective. This is due to their data-driven nature. There is no guarantee for the extrapolation accuracy, so it is not recommended to perform prediction close to or out of the sampling limit.

The GEK model can predict the gradient as well. Using Eq. (15) we can get the gradient in the original space at the test point. Figure 15 shows the comparison between gradients calculated by the adjoint solver (labeled “real”) and predicted by the GRK (labeled “predict”) at three test points. The predicted gradient is of satisfactory accuracy. It is a very interesting result. Although the linear assumption is not valid in a large parameter range, the gradient reveals the local searching direction in the optimization process. However, it should be noted that the performance of gradient prediction is highly problem specific. The predicted gradient of the loss coefficient is not accurate, for instance. The accuracy is affected by the relationship between gradients and BCs and should be checked in advance. In general, with varying gradients, the ordinary kriging model is recommended to predict objectives for its accuracy and stability. If the gradient prediction is needed, the GEK is a good option.



b) Bases for the mass flow rate

Fig. 11 First five bases given by the ASM predictor.

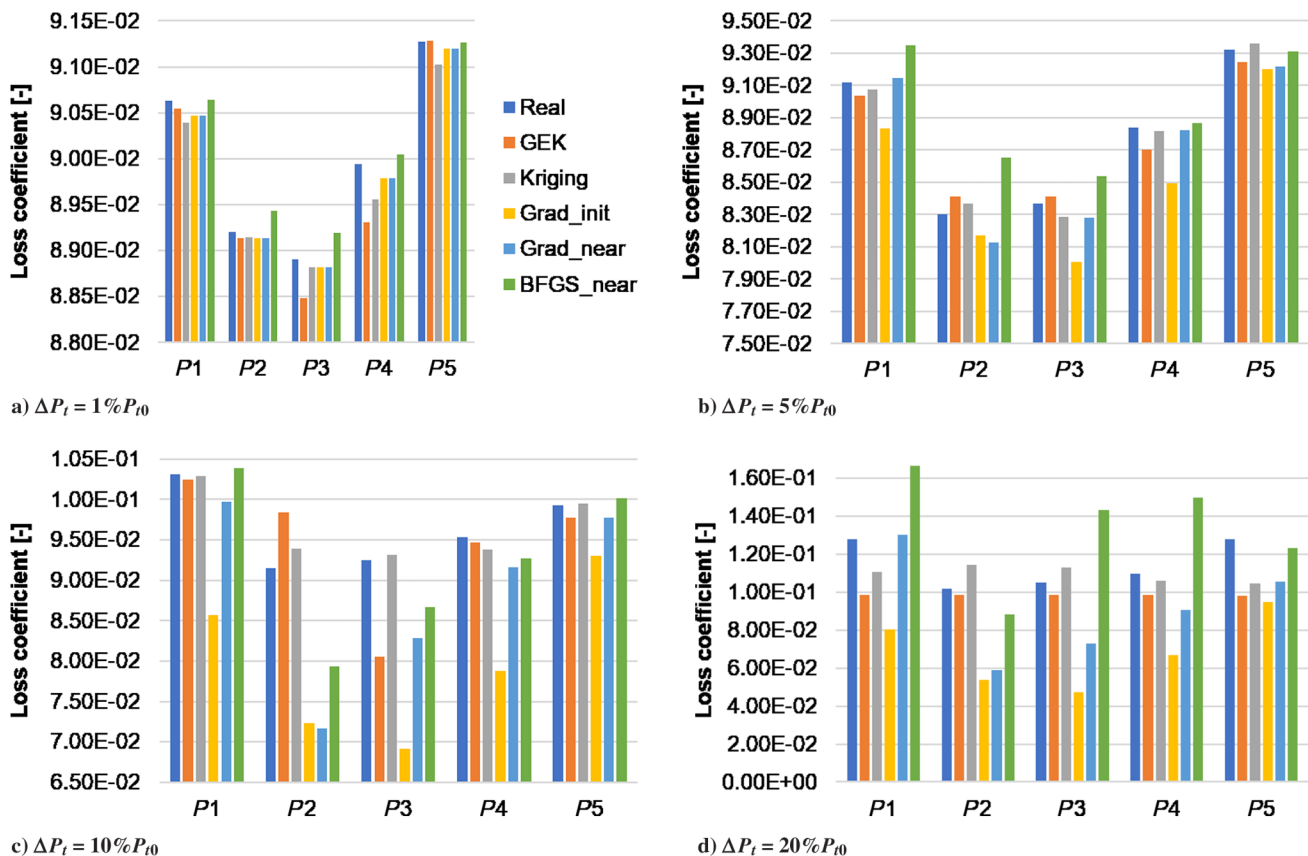


Fig. 12 Prediction of several models for loss coefficient.

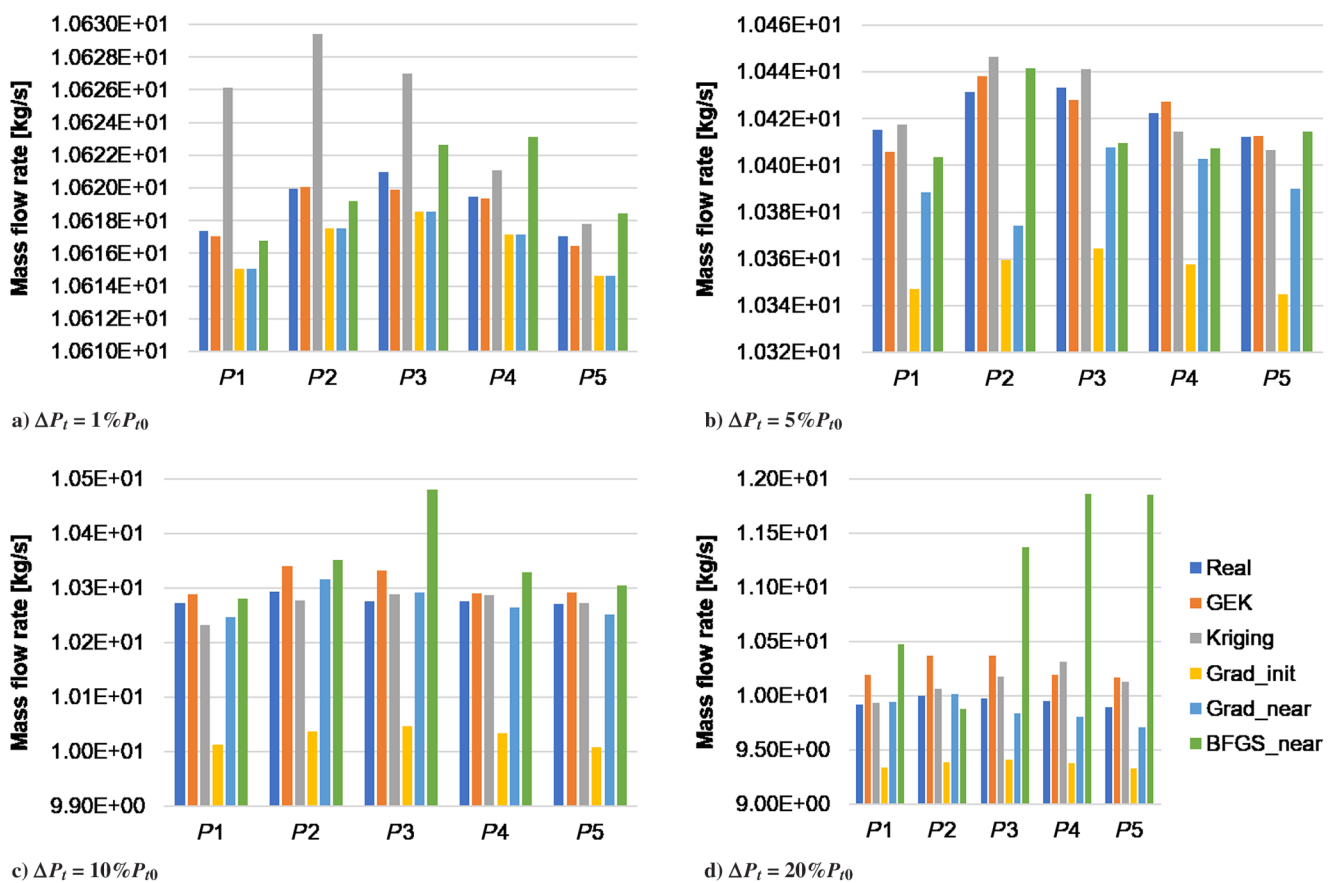


Fig. 13 Prediction of several models for mass flow rate.

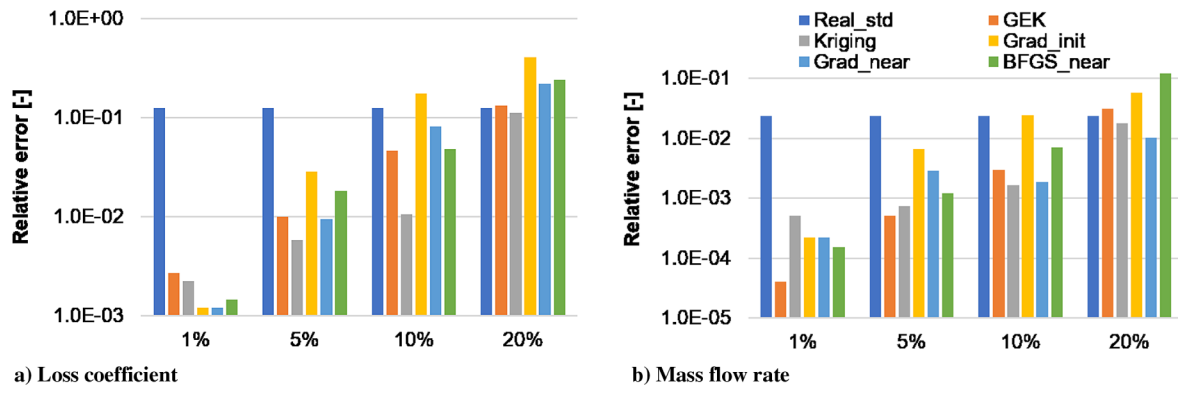
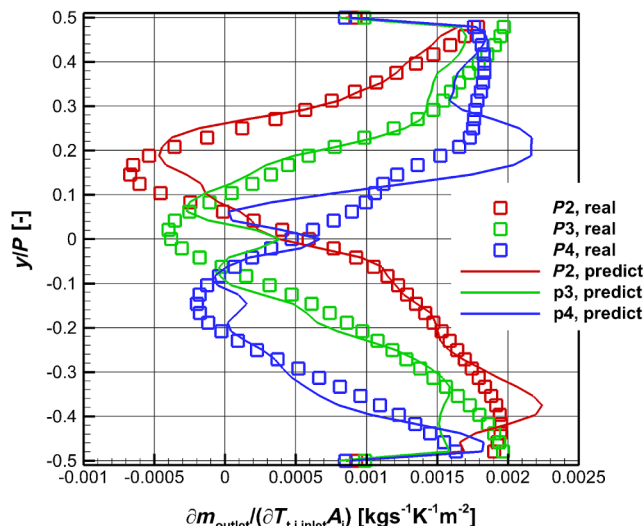


Fig. 14 Summary of relative errors with different models.

Fig. 15 Sensitivity of mass flow rate to inlet total pressure, $\Delta P_t = 5\% P_{t0}$.

V. Conclusions

An adjoint-based global BC sensitivity analysis is conducted in this work. The gradients of the performance metric with respect to BCs, which are obtained by the discrete adjoint method, are used to reveal the flow mechanisms and guide engineering designs. The strength of this gradient-based analysis is the ability to show the spatially varying sensitivity, which is difficult for the conventional comparison-based method. The gradient is inherently local information, so it is strongly recommended to check the variance property of gradients when conducting gradient-based sensitivity analysis. When the gradient is invariant across the parameter space, the linear assumption is globally valid, and the derivatives can be directly used for prediction. It is the ideal situation, where the relationship between objectives and BCs is linear. It is interesting that some gradients are almost invariant within the parameter space. In this case, the computational cost in studying the combustor/turbine interaction is drastically reduced and contains only one direct and one adjoint simulation.

When the gradient varies, a random sampling method that is based on the Gaussian process is put forward to reduce the degree of freedom. Based on these samples, the ASM strategy is introduced to reduce the dimension. Several methods that make use of state vectors or gradients are tested to predict the objective. Because of the data-driven nature of the prediction, the prediction should not exceed the sampling parameter range. The ordinary kriging model is recommended for its accuracy and stability. The GEK model is accurate for small BC variations, and it is able to predict the gradient that can be used to determine the searching direction. Therefore, for small BC variations, the GEK is a good choice. The method

presented here offers a paradigm of gradient-based global sensitivity analysis, which extends the traditional BC sensitivity analysis. Similar methods can be used to study the effect of spatially distributed source terms or model parameters.

Besides, conclusions related to this particular IGV configuration are as follows. There exist two regions at the inlet where the sensitivity of the vane temperature to the inlet total temperature is negative, meaning that adding a hot streak here can reduce the vane temperature. Based on the direct comparison and the gradient, the total pressure valley should face the vane instead of the passage to reduce loss and keep the mass flow rate.

Acknowledgments

This work was supported by the National Natural Science Foundation of China (No. 51876098), the National Science and Technology Major Project (No. J2019-II-0008-0028), and Tsinghua University Initiative Scientific Research Program. This research was also sponsored by the Open Fund from Science and Technology on Thermal Energy and Power Laboratory (TPL2018B05). Xingjian Wang of Tsinghua University is appreciated for his advice on sampling. Peng Yin of Tsinghua University is appreciated for his contribution to the gradient-enhanced kriging code.

References

- [1] Li, Y., Su, X., and Yuan, X., "The Effect of Mismatching Between Combustor and HP Vanes on the Aerodynamics and Heat Load in a 1-1/2 Stages Turbine," *Aerospace Science and Technology*, Vol. 86, March 2019, pp. 78–92.
<https://doi.org/10.1016/j.ast.2018.12.023>
- [2] Smith, C. I., Chang, D., and Tavoularis, S., "Effect of Inlet Temperature Non-Uniformity on High-Pressure Turbine Performance," *ASME Turbo Expo: Power for Land, Sea, and Air*, Vol. 7, Turbomachinery, Parts A, B, and C, ASME, New York, 2010, pp. 2465–2476.
<https://doi.org/10.1115/GT2010-22845>
- [3] Gaetani, P., and Persico, G., "Hot Streak Evolution in an Axial HP Turbine Stage," *International Journal of Turbomachinery, Propulsion and Power*, Vol. 2, No. 2, 2017, pp. 1–18.
<https://doi.org/10.3390/ijtp2020006>
- [4] Wang, Z., Liu, Z., and Feng, Z., "Influence of Mainstream Turbulence Intensity on Heat Transfer Characteristics of a High Pressure Turbine Stage With Inlet Hot Streak," *Journal of Turbomachinery*, Vol. 138, No. 4, 2015, Paper 041005.
<https://doi.org/10.1115/1.4032062>
- [5] Su, X., and Yuan, X., "Adjoint Boundary Sensitivity Method to Assess the Effect of Nonuniform Boundary Conditions," *Chinese Journal of Aeronautics*, Vol. 35, No. 2, 2021, pp. 12–16.
<https://doi.org/10.1016/j.cja.2021.04.029>
- [6] Constantine, P. G., Dow, E., and Wang, Q., "Active Subspace Methods in Theory and Practice: Applications to Kriging Surfaces," *SIAM Journal on Scientific Computing*, Vol. 36, No. 4, 2014, pp. A1500–A1524.
<https://doi.org/10.1137/130916138>
- [7] Li, J., Cai, J., and Qu, K., "Surrogate-Based Aerodynamic Shape Optimization with the Active Subspace Method," *Structural and Multi-disciplinary Optimization*, Vol. 59, No. 2, 2019, pp. 403–419.
<https://doi.org/10.1007/s00158-018-2073-5>

- [8] Seshadri, P., Shahpar, S., Constantine, P., Parks, G., and Adams, M., “Turbomachinery Active Subspace Performance Maps,” *Journal of Turbomachinery*, Vol. 140, No. 4, 2018, Paper 041003.
<https://doi.org/10.1115/1.4038839>
- [9] Sieverding, C. H., Richard, H., and Desse, J.-M., “Turbine Blade Trailing Edge Flow Characteristics at High Subsonic Outlet Mach Number,” *Journal of Turbomachinery*, Vol. 125, No. 2, 2003, pp. 298–309.
<https://doi.org/10.1115/1.1539057>
- [10] Economou, T. D., Palacios, F., Copeland, S. R., Lukaczyk, T. W., and Alonso, J. J., “SU2: An Open-Source Suite for Multiphysics Simulation and Design,” *AIAA Journal*, Vol. 54, No. 3, 2016, pp. 828–846.
<https://doi.org/10.2514/1.J053813>
- [11] Jameson, A., “Origins and Further Development of the Jameson–Schmidt–Turkel Scheme,” *AIAA Journal*, Vol. 55, No. 5, 2017, pp. 1487–1510.
<https://doi.org/10.2514/1.J055493>
- [12] Spalart, P., and Allmaras, S., “A One-Equation Turbulence Model for Aerodynamic Flows,” *30th Aerospace Sciences Meeting and Exhibit*, AIAA Paper 1992-0439, 1992.
<https://doi.org/10.2514/6.1992-439>
- [13] Albring, T. A., Sagebaum, M., and Gauger, N. R., “Efficient Aerodynamic Design Using the Discrete Adjoint Method in SU2,” *17th AIAA/ISSMO Multidisciplinary Analysis and Optimization Conference*, AIAA Paper 2016-3518, 2016.
<https://doi.org/10.2514/6.2016-3518>
- [14] Sagebaum, M., Albring, T. A., and Gauger, N. R., “High-Performance Derivative Computations Using CoDiPack,” *ACM Transactions on Mathematical Software (TOMS)*, Vol. 45, No. 4, 2019, pp. 1–26.
<https://doi.org/10.1145/3356900>
- [15] Jameson, A., “Aerodynamic Design via Control Theory,” *Journal of Scientific Computing*, Vol. 3, No. 3, 1988, pp. 233–260.
<https://doi.org/10.1007/BF01061285>
- [16] Jameson, A., and Ou, K., “50 years of Transonic Aircraft Design,” *Progress in Aerospace Sciences*, Vol. 47, No. 5, 2011, pp. 308–318.
<https://doi.org/10.1016/j.paerosci.2011.01.001>
- [17] Han, Z.-H., Görtz, S., and Zimmermann, R., “Improving Variable-Fidelity Surrogate Modeling via Gradient-Enhanced Kriging and a Generalized Hybrid Bridge Function,” *Aerospace Science and technology*, Vol. 25, No. 1, 2013, pp. 177–189.
<https://doi.org/10.1016/j.ast.2012.01.006>
- [18] Han, Z.-H., Zhang, Y., Song, C.-X., and Zhang, K.-S., “Weighted Gradient-Enhanced Kriging for High-Dimensional Surrogate Modeling and Design Optimization,” *AIAA Journal*, Vol. 55, No. 12, 2017, pp. 4330–4346.
<https://doi.org/10.2514/1.J055842>
- [19] Paulson, C., and Ragkousis, G., “pyKriging: A Python Kriging Toolkit,” 2015.
<https://doi.org/10.5281/zenodo.21389>

J. Larsson
Associate Editor